

## Evolution of MHD turbulence in the expanding solar wind: residual energy and intermittency

CHEN SHI (时辰) <sup>1</sup>, NIKOS SIOULAS <sup>1</sup>, ZESEN HUANG (黄泽森) <sup>1</sup>, MARCO VELLI <sup>1</sup>, ANNA TENERANI <sup>2</sup> AND  
VICTOR RÉVILLE <sup>3</sup>

<sup>1</sup>*Department of Earth, Planetary, and Space Sciences, University of California, Los Angeles  
Los Angeles, CA 90095, USA*

<sup>2</sup>*Department of Physics, The University of Texas at Austin,  
TX 78712, USA*

<sup>3</sup>*IRAP, Université Toulouse III - Paul Sabatier, CNRS, CNES, Toulouse, France*

### ABSTRACT

We conduct 3D magnetohydrodynamic (MHD) simulations of decaying turbulence in the solar wind context. To account for the spherical expansion of the solar wind, we implement the expanding box model. The initial turbulence comprises uncorrelated counter-propagating Alfvén waves and exhibits an isotropic power spectrum. Our findings reveal the consistent generation of negative residual energy whenever nonlinear interactions are present, independent of the normalized cross helicity  $\sigma_c$ . The spherical expansion facilitates this process. The resulting residual energy is primarily distributed in the perpendicular direction, with  $[S_2(\mathbf{b}) - S_2(\mathbf{u})] \propto l_\perp$  or equivalently  $-E_r \propto k_\perp^{-2}$ . Here  $S_2(\mathbf{b})$  and  $S_2(\mathbf{u})$  are second-order structure functions of magnetic field and velocity respectively. In most runs,  $S_2(\mathbf{b})$  develops a scaling relation  $S_2(\mathbf{b}) \propto l_\perp^{1/2} (E_b \propto k_\perp^{-3/2})$ . In contrast,  $S_2(\mathbf{u})$  is consistently shallower than  $S_2(\mathbf{b})$ , which aligns with in-situ observations of the solar wind. We observe that the higher-order statistics of the turbulence, which act as a proxy for intermittency, are strongly affected by the expansion effect but have weak dependence on the initial  $\sigma_c$ . Generally, the intermittency is more pronounced when the expansion effect is present. Finally, we find that in our simulations although the negative residual energy and intermittency grow simultaneously as the turbulence evolves, there is no obvious causal relation between them because they are generated on different scales.

### 1. INTRODUCTION

It has long been observed that solar wind is a highly turbulent plasma system with fluctuations on a wide range of scales (see the review by Bruno & Carbone 2013, and references therein). Studying the solar wind turbulence is of great importance because turbulence is an important power source for the heating and acceleration of solar wind (Cranmer et al. 2007; Verdini et al. 2009; Lionello et al. 2014; Cranmer et al. 2015; Van Ballegoijen & Asgari-Targhi 2016; Shoda et al. 2019; Réville et al. 2020; Magyar & Nakariakov 2021).

In the last decades, significant progresses have been made on observations, numerical simulations, and theories of the solar wind turbulence. Satellite observations reveal that in fast solar wind, the turbulence is usually highly Alfvénic, dominated by outward propa-

gating Alfvén waves (Belcher & Davis Jr 1971), while in slow solar wind, Alfvénicity of the turbulence is typically lower than the fast wind, but can be quite high in certain intervals (D’Amicis & Bruno 2015; D’Amicis et al. 2019), especially in the nascent solar wind as observed by Parker Solar Probe (Panasenco et al. 2020; Parashar et al. 2020).

Since the compressible fluctuation is typically small in the solar wind, with  $\delta n/n \lesssim 0.2$  (Shi et al. 2021) where  $n$  is the average plasma density and  $\delta n$  is the fluctuation amplitude of the density, the solar wind turbulence is treated as an incompressible MHD system in most theoretical and modeling works, where two Elsässer variables  $z^\pm = \mathbf{u} \mp \mathbf{b}$ , which are linear combinations of the velocity  $\mathbf{u}$  and magnetic field  $\mathbf{b}$  (in Alfvén speed) and represent the two counter-propagating Alfvén wave populations, are analyzed. A number of phenomenological models have been developed for the incompressible MHD turbulence. The weak ( $|\delta \mathbf{b}|/B \ll 1$ ), isotropic (in  $\mathbf{k}$  space), balanced ( $z^+ \sim z^-$ ) turbulence model (Iroshnikov 1964; Kraichnan 1965) predicts a 1D power spectrum  $E_{1D} \propto$

$k^{-3/2}$ . The weak, anisotropic, balanced model (Goldreich & Sridhar 1997) predicts a 1D power spectrum  $E_{1D} \propto k_{\perp}^{-2}$ . For strong, anisotropic turbulence, ‘‘critical balance’’ theory (Goldreich & Sridhar 1995), which balances the linear propagation timescale and the nonlinear eddy turnover timescale, predicts  $E_{1D} \propto k_{\perp}^{-5/3}$ . Based on the critical balance theory, scale-dependent dynamic alignment model (Boldyrev 2005; Perez & Boldyrev 2007) allows the spectral slope to be variable depending on how much the two Elsässer variables are aligned with each other. Compared with the balanced turbulence, imbalanced turbulence is more difficult to describe, and no simple phenomenological model has been established so far (Dobrowolny et al. 1980a,b; Grappin et al. 1983; Lithwick & Goldreich 2003; Lithwick et al. 2007; Beresnyak & Lazarian 2010). Incompressible simulations conducted by Perez & Boldyrev (2009) show that in strong turbulence the two imbalanced Elsässer variables may have similar power spectra despite of different amplitudes, while simulations conducted by Beresnyak & Lazarian (2009) show that the two Elsässer variables have very different structures.

As the phenomenological models and previous numerical simulations have successfully explained some of the satellite observations, many mysteries still remain. One of the most outstanding problems is the prevailing negative residual energy, i.e. an excess of magnetic energy over the kinetic energy, in the solar wind turbulence (Chen et al. 2013, 2020; Shi et al. 2021; Sioulas et al. 2023). Many theoretical works have been carried out (Müller & Grappin 2005; Yokoi & Hamba 2007; Wang et al. 2011; Boldyrev et al. 2012a; Gogoberidze et al. 2012; Howes & Nielson 2013) to explain the generation of a negative residual energy but they are not fully self-consistent and do not give consistent results, e.g. on spectral slope of the residual energy. In addition, although most of the phenomenological models assume self-similarity, intermittency plays a non-negligible role in MHD turbulence as it undermines the self-similarity assumption (Chandran et al. 2015; Mallet & Schekochihin 2017; Wu et al. 2023). Besides, intermittency is an important way of energy dissipation and is observed to be directly correlated with plasma heating in the solar wind (Sioulas et al. 2022a,b; Phillips et al. 2023).

In this study, we investigate, through 3D MHD simulations, turbulence evolution in the solar wind context with a focus on the residual energy and intermittency. Expanding-box-model (EBM) (Grappin & Velli 1996; Dong et al. 2014; Tenerani & Velli 2017; Shi et al. 2020, 2022; Grappin et al. 2022) was implemented because the spherical expansion of the solar wind may significantly change the turbulence evolution as it leads to anisotropic

decay of different components of the magnetic field and velocity. The paper is organized as follows. In Section 2, we describe the simulation setup. In Section 3, we present the main simulation results. In Section 4 we discuss the relation between the residual energy and intermittency. In Section 5, we summarize the paper and discuss future works.

## 2. SIMULATION SETUP

We use a 3D pseudo-spectral compressible MHD code with EBM to conduct the simulations. The algorithm of the code is described in details in (Shi et al. 2020). In all the simulations, the domain is a rectangular box with initial size  $(5R_s)^3$  ( $R_s$  is the solar radius) and grid number  $512^3$ . Besides de-aliasing in  $\mathbf{k}$ -space, explicit resistivity  $\eta = 2 \times 10^{-5}$  and viscosity  $\nu = 2 \times 10^{-5}$  are implemented to maintain numerical stability. We note that, because the code is based on MHD equation in conservation form, the viscosity is implemented as  $\partial_t(\rho\mathbf{u})_{\mathbf{k}} \sim -k^2\nu(\rho\mathbf{u})_{\mathbf{k}}$  where  $(\rho\mathbf{u})_{\mathbf{k}}$  is Fourier mode  $\mathbf{k}$  of the conserved variable  $\rho\mathbf{u}$ .

The initial fields consist of uniform background and fluctuations. The background fields are  $\rho_0 = B = 1$ ,  $P_0 = 0.1006$ , with normalization units  $\bar{n} = 200 \text{ cm}^{-3}$ ,  $\bar{B} = 250 \text{ nT}$ , and subsequently  $\bar{P} = \bar{B}^2/\mu_0 = 49.7 \text{ nPa}$  where  $\mu_0$  is the permeability. The background magnetic field is within the equatorial plane ( $x - y$  plane) and has an angle of  $8.1^\circ$  with respect to the radial direction ( $\hat{e}_x$ ), so that in simulations with expansion this angle increases to about  $45^\circ$  at 1AU. The adiabatic index is  $\gamma = 1.5$  instead of  $5/3$  to prevent the plasma temperature from cooling too fast in the runs with expansion. This choice only slightly modifies the thermodynamics and is not expected to impact our results significantly.

Fluctuations of velocity and magnetic field with 3D isotropic power spectra are added on top of the background such that the reduced 1D spectra roughly follow  $|k|^{-1.3}$ . The initial fluctuations are Alfvénic: for any wave mode  $\mathbf{k}$ , there is  $\mathbf{b}_{\mathbf{k}} \propto (\mathbf{k} \times \mathbf{B})$ , where  $\mathbf{b}_{\mathbf{k}}$  is the magnetic field fluctuation of wave-vector  $\mathbf{k}$ . Usually, we use the normalized cross helicity  $\sigma_c$  and normalized residual energy  $\sigma_r$  to measure the Alfvénicity of the turbulence, and they are defined as

$$\sigma_c = \frac{E_+ - E_-}{E_+ + E_-}, \sigma_r = \frac{E_k - E_b}{E_k + E_b} \quad (1)$$

where  $E_{\pm}$  represent the energy of the outward/inward Alfvén waves ( $z^{\pm}$ ) and  $E_{k,b}$  represent the kinetic and magnetic energies of the fluctuations. We note that  $\sigma_c$  measures the correlation between the velocity and magnetic field, and  $\sigma_r$  measures the correlation between the two Elsässer variables. At initialization, we control  $\sigma_c$

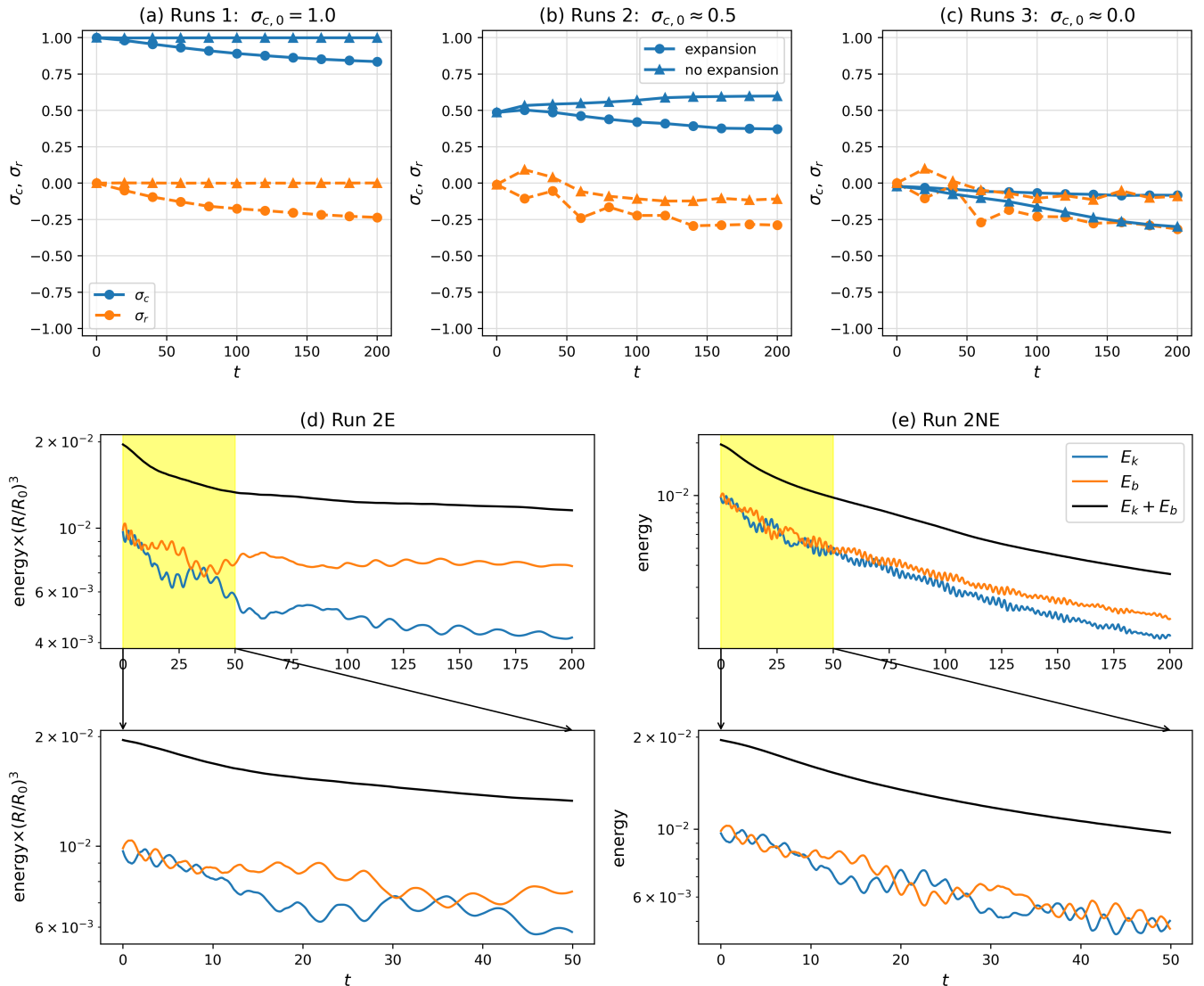


**Figure 1.** Panels (a)-(c): Evolution of  $\sigma_c$  (blue) and  $\sigma_r$  (orange dashed) in Runs 1 (a), Runs 2 (b), and Runs 3 (c). Lines with circles are runs with expansion, and lines with triangles are runs without expansion. Panels (d) & (e): Evolution of kinetic energy (blue), magnetic energy (orange), and total energy (black) with high-resolution output for Run 2E and Run 2NE. Bottom row shows blow-ups of the yellow-shaded regions in the top row. For Run 2E, we have multiplied the energies by  $(R/R_0)^3$  (according to WKB theory) to compensate the energy decay due to expansion.

by varying the correlation between the velocity fluctuation and magnetic field fluctuation, and we keep  $\sigma_r$  to be exactly zero.

The root-mean-square of the magnetic field fluctuation is  $b_{rms}/B \approx 0.14$  for all the runs. Thus, the nonlinear eddy turnover time is estimated to be  $\tau_{nl} \sim L/2\pi b_{rms} \approx 5.7$  and the effective Reynolds number  $Re$  (and Lundquist number  $S$ ) is  $Re = S \approx Lb_{rms}/\nu \approx 3.5 \times 10^4$ . We note that because the background plasma has quite low  $\beta$  ( $\approx 0.2$ ) as we want the configuration to be close to the realistic solar wind in the inner heliosphere (Artemyev et al. 2022), the fluctuation level cannot be too strong, otherwise the simulation will be

unstable due to formation of shocks. In contrast, (Dong et al. 2014) and (Grappin et al. 2022) added strong turbulence (with  $b_{rms}/B \approx 1$ ) to their simulations by adopting large  $\beta$  values.

In the runs with expansion, the initial radial location of the simulation domain is  $R_0 = 30R_s$ , and the radial speed of the box is  $U_r = 1.167$  with normalization unit  $\bar{U} = \bar{B}/\sqrt{\mu_0 m_p \bar{n}} = 385.6$  km/s where  $m_p$  is the proton mass. We carry out six runs which are divided into three groups: Runs (1E, 1NE), Runs (2E, 2NE), and Runs (3E, 3NE). Here ‘‘E’’ and ‘‘NE’’ stand for ‘‘expansion’’ and ‘‘no expansion’’ respectively. Runs 1 have  $\sigma_{c,0} = 1$ ,

Runs 2 have  $\sigma_{c,0} \approx 0.5$ , and Runs 3 have  $\sigma_{c,0} \approx 0$  where  $\sigma_{c,0}$  is the initial normalized cross helicity.

### 3. RESULT

#### 3.1. Evolution of $\sigma_c$ and $\sigma_r$

In Figure 1, panels (a)-(c) show the time evolution of  $\sigma_c$  (blue) and  $\sigma_r$  (orange dashed) in Runs 1, Runs 2, and Runs 3 respectively. Lines with circles are runs with expansion and lines with triangles are runs without expansion. With expansion,  $|\sigma_c|$  in general decreases with time (Runs 1E & 2E) because of the reflection of the outward propagating Alfvén waves due to the inhomogeneity of the background fields (Heinemann & Olbert 1980; Velli et al. 1991). Without expansion, Run 1NE ( $\sigma_{c,0} = 1$ ) does not evolve because nonlinear interaction is absent in the exactly Alfvénic status. In Run 2NE ( $\sigma_{c,0} \approx 0.5$ ),  $\sigma_c$  increases gradually, possibly because of the “dynamic alignment” (Dobrowolny et al. 1980a,b), i.e. an initially imbalanced turbulence tends to evolve toward purely Alfvénic status because the energy decay rates of the two counter-propagating Alfvén wave populations are similar. In Run 3E,  $\sigma_c$  is slightly negative but stays at very low absolute values because of the competition between the dynamic alignment which tends to increase  $|\sigma_c|$  and the expansion effect which tends to decrease  $|\sigma_c|$ . We note that for Runs 3 whether  $\sigma_c$  evolves toward positive or negative is very sensitive to the initial condition.

$\sigma_r$  evolves toward negative values in all the runs except for Run 1NE, indicating that nonlinear interaction naturally generates negative residual energy (Grappin et al. 1983; Yokoi & Hamba 2007; Gogoberidze et al. 2012; Wang et al. 2011; Boldyrev et al. 2012a; Howes & Nielson 2013), consistent with the prevailing negative residual energy observed in the solar wind (Chen et al. 2013, 2020; Shi et al. 2021). In addition, it is clear that  $\sigma_r$  decays faster in runs with expansion than those without expansion. This may be attributed to the fact that the expansion-induced decay of magnetic energy is slower than that of kinetic energy (Dong et al. 2014; Shi et al. 2022), i.e.

$$b_{\perp}^2 \propto R^{-2}, \rho u_{\perp}^2 \propto R^{-4} \quad (2)$$

in the absence of any coupling between  $\mathbf{b}$  and  $\mathbf{u}$ . In Panels (d) and (e), we show the time evolution of kinetic (blue) and magnetic (orange) energies in Run 2E and Run 2NE respectively with high time resolution. Total energy is also shown as the black curves. For Run 2E we have multiplied the energies by  $(R/R_0)^3$  to compensate the energy decay due to solar wind expansion (the WKB theory, Belcher 1971). We observe high-frequency oscillations of  $E_k$  and  $E_b$ , which are anti-correlated so

that the total energy does not oscillate. This oscillation is clearly a result of the wave propagation effect (Wang et al. 2011). From panel (e), we can estimate the oscillation period is roughly  $T \approx 2.5 \approx L_x/2B_0$ , and from panel (d) we see that the period increases gradually because the expansion increases the crossing time of Alfvén waves through the simulation domain. Panels (d) and (e) indicate that the magnetic energy excess is built up over multiple wave crossing times.

#### 3.2. Second-order structure functions

We then investigate the second-order structure functions of different fields. The  $q$ -th order structure function of a field  $\mathbf{b}(\mathbf{x})$  is defined as

$$S_q(\mathbf{b}, \mathbf{l}) = \langle |\mathbf{b}(\mathbf{x} + \mathbf{l}) - \mathbf{b}(\mathbf{x})|^q \rangle_{\mathbf{x}} \quad (3)$$

where  $\mathbf{l}$  is a given spatial increment, and  $\langle \rangle_{\mathbf{x}}$  means ensemble average or equivalently average over the whole simulation domain. Especially, the second-order structure function  $S_2$  measures the mean-square value of the fluctuation on scale  $\mathbf{l}$ . One important relation is that, if  $S_2$  scales exponentially with the spatial increment such that  $S_2 \propto l^\alpha$ , the power spectrum of the field obeys the scaling  $E \propto k^{-(\alpha+1)}$  (Montroll & Shlesinger 1982).

Figure 2 shows  $S_2$  of velocity (blue), magnetic field (orange dashed) and negative residual energy (magnetic energy minus kinetic energy, green dotted) at the end of the simulations ( $t = 200$ ), when turbulence has evolved a sufficient time. Panels (a)-(c) correspond to Run 1E ( $\sigma_{c,0} = 1$ ) with  $\mathbf{l} = l_x \hat{e}_x$ ,  $\mathbf{l} = l_y \hat{e}_y$ , and  $\mathbf{l} = l_z \hat{e}_z$  respectively. Anisotropy among the three directions is clearly observed. Residual energy is generated only along the  $z$  direction, i.e. the direction perpendicular to both the background magnetic field and radial direction. Along  $l_x$  (radial and initially quasi-parallel), no clear power-law relation is established. Along  $l_y$ , an extended power-law part with a slope slightly smaller than 0.5 forms. Along  $l_z$ , we get  $S_2(\mathbf{b}) \propto l_z^{0.5}$  and  $S_2(\mathbf{u}) \propto l_z^{0.25}$ , i.e. the velocity field has a shallower power spectrum than the magnetic field, consistent with satellite observations (Chen et al. 2020; Shi et al. 2021), though the spectral slopes from the simulations are systematically shallower than satellite observations which show that the magnetic field and velocity power spectra have slopes of  $-5/3$  and  $-3/2$  on average (Chen et al. 2013). From panel (c), we can see that the negative residual energy has a power-law scaling  $S_2 \propto l_z$ , i.e.  $-E_r \propto k_z^{-2}$ . This spectral slope is consistent with the WIND observation (Chen et al. 2013) as well as the prediction given by the Eddy Damped Quasi Normal Markovian (EDQNM) model of isotropic

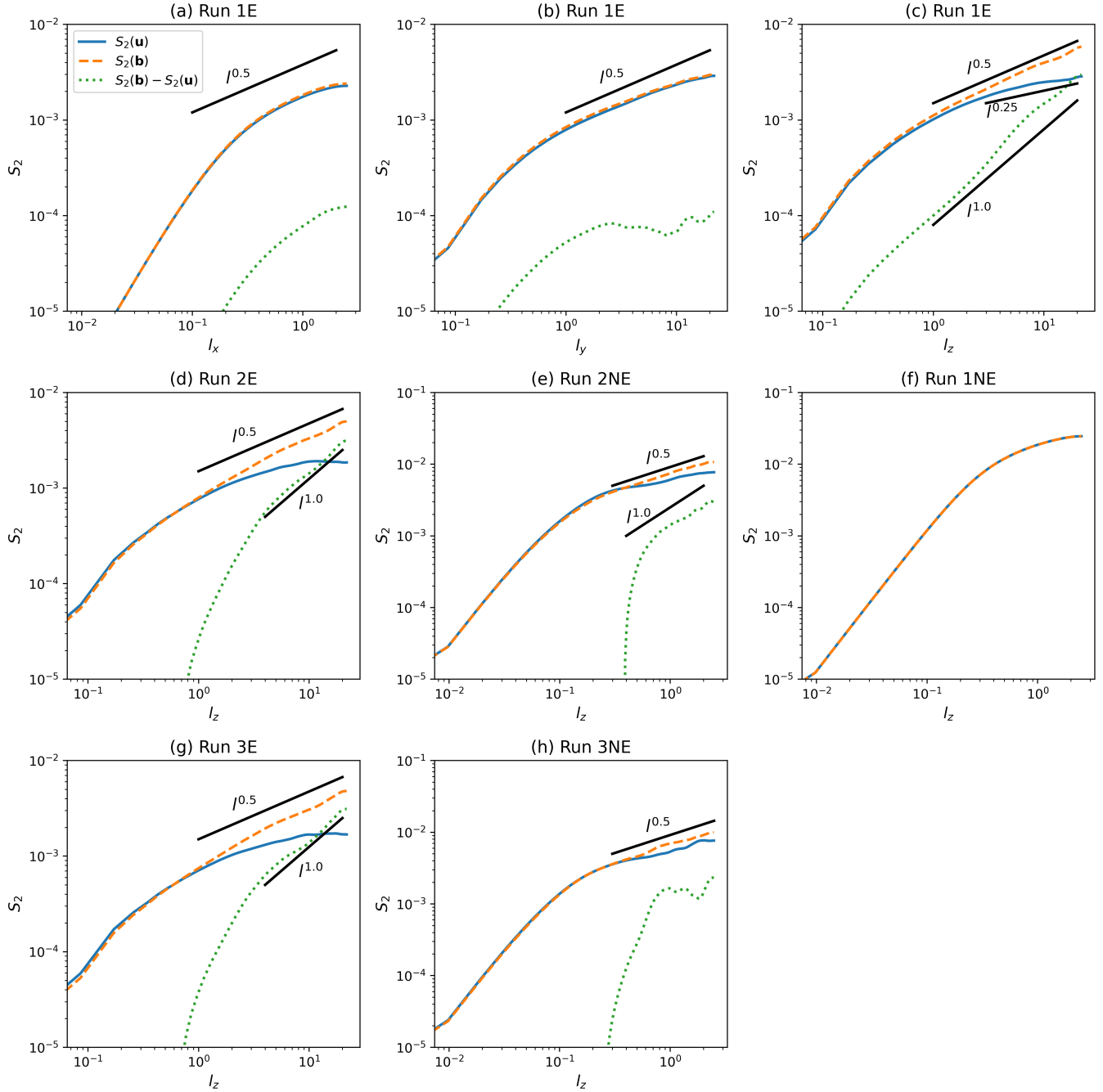


**Figure 2.** Second-order structure functions of velocity  $S_2(\mathbf{u})$  (blue), magnetic field  $S_2(\mathbf{b})$  (orange dashed), and the difference between them  $S_2(\mathbf{b}) - S_2(\mathbf{u})$  (green dotted) at the end of simulations ( $t = 200$ ). Panels (a)-(c) are Run 1E with  $\mathbf{l}$  along  $x$ ,  $y$ , and  $z$  directions respectively. Panels (d)-(h) are the other five runs with  $\mathbf{l} = l_z \hat{e}_z$ .

MHD turbulence (Grappin et al. 1983)<sup>1</sup> and the model by (Boldyrev et al. 2012a). However, we note that there is so far no self-consistent theory for the spectral slope of residual energy, and different models can give different

results. For example, Wang et al. (2011) shows, through analytic calculation, that in the weak turbulence scenario negative residual energy is produced and follows  $-E_r \propto k_\perp^{-1}$ . The EDQNM model for strong, anisotropic MHD turbulence Gogoberidze et al. (2012) also shows that negative residual energy arises due to nonlinear interaction but its spectrum follows  $-E_r \propto k_\perp^{-5/3}$ .

<sup>1</sup> In (Grappin et al. 1983), the sign of the residual energy is not defined.

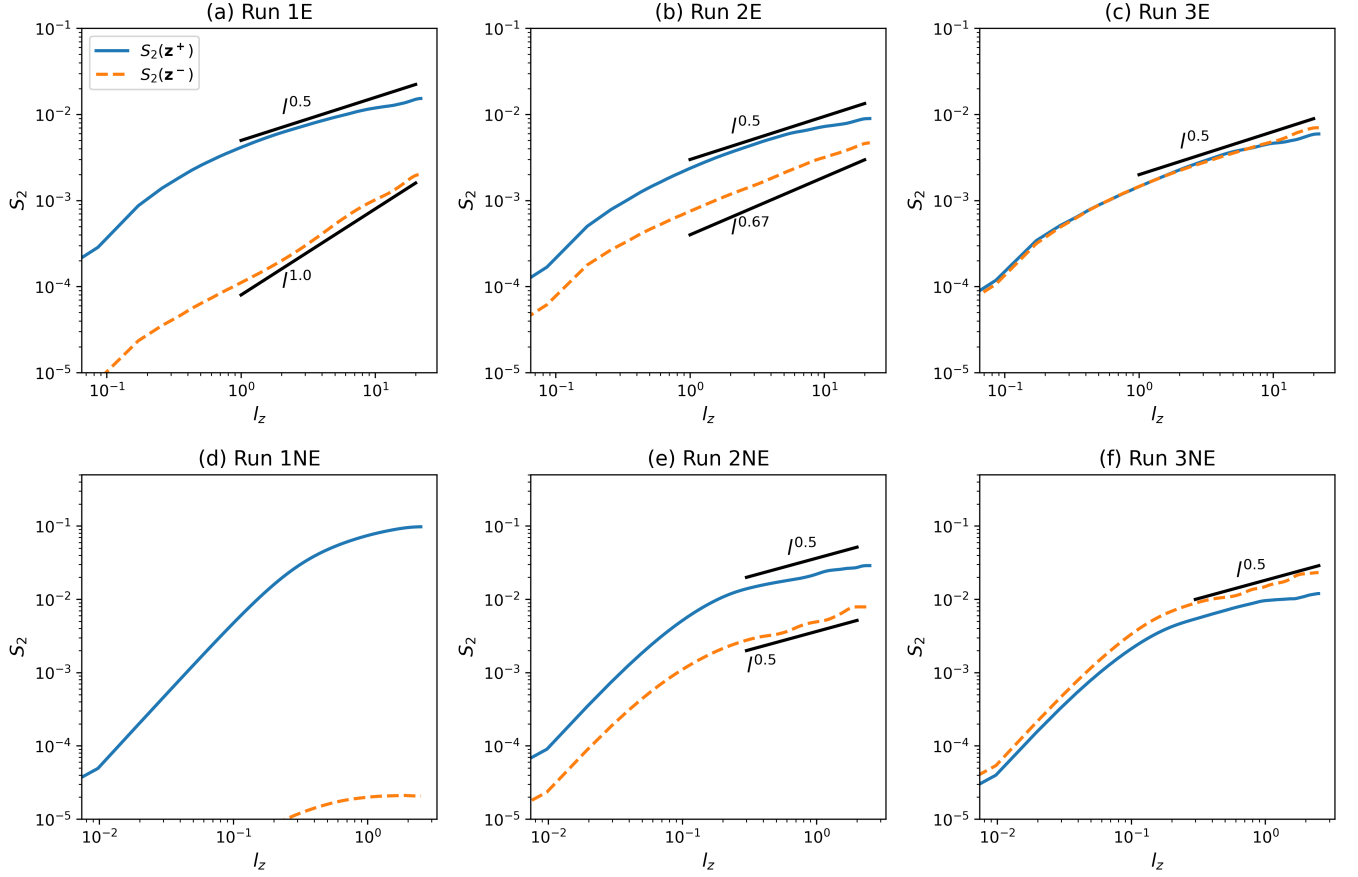


**Figure 3.** Second-order structure functions of Elsässer variables  $S_2(\mathbf{z}^+)$  (blue) and  $S_2(\mathbf{z}^-)$  (orange dashed) at the end of simulations ( $t = 200$ ).

As  $\hat{e}_z$  is the dimension in which the most interesting processes take place, we only show  $S_2(l_z)$  for the other five runs in panels (d)-(h). Run 1NE does not undergo any nonlinear evolution as discussed in Section 3.1. Runs 2 and Runs 3 show quite similar results with Run 1E, with  $S_2(\mathbf{b}) \propto l_z^{0.5}$  and shallower  $S_2(\mathbf{u})$ , though in Run 2NE and Run 3NE  $S_2(\mathbf{u})$  is steeper than runs with expansion. We note that the negative residual energy has a clear  $S_2 \propto l_z$  scaling relation in all the runs except for Run 1NE and Run 3NE, indicating that the residual energy spectrum does not depend on  $\sigma_c$  and the expansion effect significantly.

In Figure 3, we show  $S_2(l_z)$  of  $\mathbf{z}^+$  (blue) and  $\mathbf{z}^-$  (orange dashed) at the end of the six runs.  $S_2(\mathbf{z}^+)$  has very similar shapes, i.e. with a slope slightly shallower than 0.5, in all the runs except for Run 1NE. However, the slope of  $S_2(\mathbf{z}^-)$  behaves differently from  $S_2(\mathbf{z}^+)$ . For Run 2NE and Run 3NE, it is roughly 0.5, but for runs with expansion, it is strongly affected by  $\sigma_c$ . For Run 1E ( $\sigma_{c,0} = 1$ ),  $S_2(\mathbf{z}^-) \propto l_z$ ; for Run 2E ( $\sigma_{c,0} \approx 0.5$ ),  $S_2(\mathbf{z}^-) \propto l_z^{2/3}$ ; for Run 3E ( $\sigma_{c,0} \approx 0$ ),  $S_2(\mathbf{z}^-) \propto l_z^{0.5}$ . That is to say, the perpendicular spectrum of  $\mathbf{z}^-$  is

steeper when the turbulence is more imbalanced. Similar result was found in the EBM simulations conducted by Grappin et al. (2022). In previous numerical works without expansion effect (Perez & Boldyrev 2009; Perez et al. 2012), the  $\mathbf{z}^-$  spectral slope is  $E \sim k_{\perp}^{-1.5}$  for both balanced and imbalanced turbulence, consistent with our results, while the  $\mathbf{z}^+$  spectrum is steeper than  $\mathbf{z}^-$ . This inconsistency may be a result of the difference in the simulation setup as Perez & Boldyrev (2009) and Perez et al. (2012) implement driving forces for the turbulence, but our simulations contain decaying turbulence. We note that, Grappin et al. (2022), through a comprehensive parametric study, find that the spectral slopes of  $\mathbf{z}^{\pm}$  can be affected by various factors, including the initial spectral slopes and the turbulence strength.

### 3.3. Higher-order statistics of the magnetic field

It is well known that intermittency develops in MHD turbulence, generating local structures in magnetic field and velocity. One good measure of the intermittency is the scaling exponents of structure functions. For homogeneous turbulence, distribution of the fluctuations is

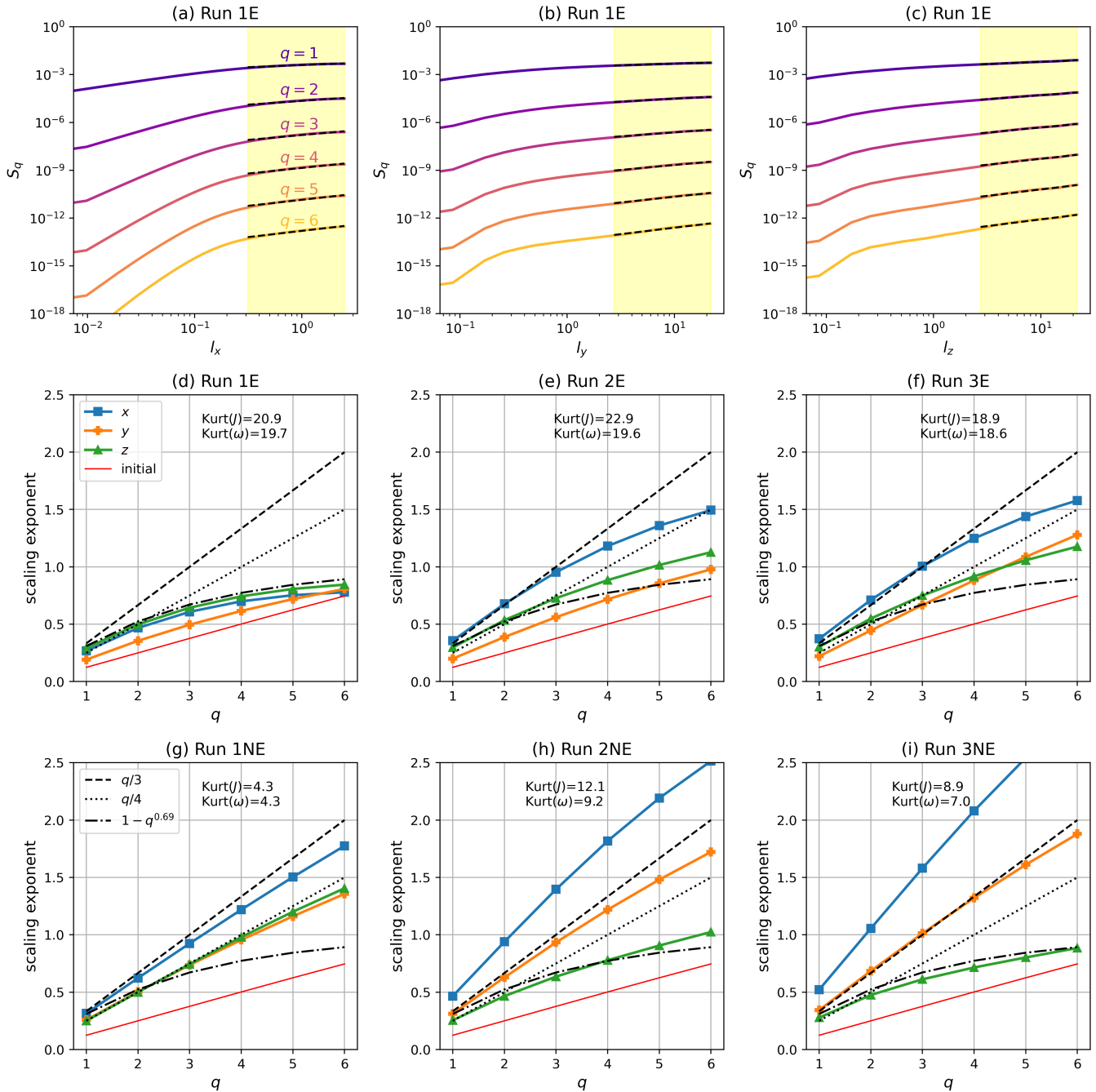


**Figure 4.** Panels (a)-(c): Structure functions of magnetic field  $S_q(\mathbf{b}, \mathbf{l})$  for  $\mathbf{l} = l_x \hat{e}_x$ ,  $\mathbf{l} = l_y \hat{e}_y$ , and  $\mathbf{l} = l_z \hat{e}_z$  at the end of Run 1E ( $t = 200$ ). Curves for  $q = 1 - 6$  are plotted. Yellow shades mark the ranges of scales used for fitting the structure functions. Panels (d)-(i): Scaling exponents as functions of  $q$  along  $x$  (blue square),  $y$  (orange cross), and  $z$  (green triangle) directions. In each panel, red line shows the initial status ( $t = 0$ ). The three black lines are  $q/3$ ,  $q/4$ , and  $1 - q^{0.69}$  for reference.

supposed to be Gaussian, in which case the slope (“scaling exponent”) of the  $q$ -th order structure function is a linear function of  $q$ , i.e. “mono-fractal.” With intermittency, the slope becomes a nonlinear function of  $q$ , i.e. “multi-fractal,” due to the non-Gaussian distribution of fluctuations. Observations have revealed that the mag-

netic field fluctuations in the solar wind are typically multi-fractal (e.g. Sioulas et al. 2022c).

In panels (a)-(c) of Figure 4, we show the magnetic field structure functions  $S_q(\mathbf{b}, \mathbf{l})$  at the end of Run 1E as an example. For each curve, we apply linear fitting to the range  $L/16 \leq l \leq L/2$ , which is marked by the yellow shades, and get the scaling exponents.

In panels (d)-(i), we show the fitted scaling exponents at the end of the six runs. Here the blue curves with squares correspond to  $l_x$ , the orange curves with diamonds correspond to  $l_y$ , and the green curves with triangles correspond to  $l_z$ . For references, the black dashed line shows  $q/3$ , which is the Kolmogorov turbulence model, the black dotted line shows  $q/4$ , which is the Iroshnikov-Kraichnan turbulence model, and the black dashed-dotted line is  $1 - q^{0.69}$ , which is a multifractal intermittency model based on strong, balanced turbulence assumption (Chandran et al. 2015). We note that the result for Run 1NE is unreliable because the structure functions barely develop a power-law in this run. Anisotropy among  $x$ ,  $y$ , and  $z$  axes as well as multifractality are clearly observed in all the runs. Inspecting the results on  $l_z$ , we find that the scaling exponents in Run 3NE roughly follow the prediction by (Chandran et al. 2015) as expected. Interestingly, in Run 1E (very imbalanced turbulence with expansion), the scaling exponents also follow the prediction by (Chandran et al. 2015) which, however, is based on balanced turbulence assumption.

Another useful quantification of intermittency is Kurtosis of current density  $J = |\nabla \times \mathbf{B}|$  and vorticity  $\omega = |\nabla \times \mathbf{u}|$ , which measure how strong the local current sheets and local vortices are. The Kurtosis of a quantity is defined as

$$\text{Kurtosis}(f) = \frac{\langle f^4 \rangle_{\mathbf{x}}}{\langle f^2 \rangle_{\mathbf{x}}^2}$$

where again  $\langle \cdot \rangle_{\mathbf{x}}$  stands for average over the simulation domain. We calculate the two quantities for each run and write them in panels (d)-(i) of Figure 4. Moreover, in Figure 5, we show the time evolution of Kurtosis( $J$ ) (blue circle) and Kurtosis( $\omega$ ) (orange triangle) in different runs. Note that Run 1NE results are shown as the grey dashed lines in top left panel. Compare Kurtosis in different runs, we find that intermittency is obviously stronger in runs with expansion, possibly because of the selective decay of different components of the magnetic field and velocity which gives rise to small-scale structures Dong et al. (2014). In addition, no significant discrepancy in Kurtosis is observed among runs with different  $\sigma_c$ . This is interesting because one expects that for balanced turbulence, the nonlinear interaction is stronger and thus should generate more intermittency. Theory of intermittency for imbalanced turbulence and an observational study to compare the intermittency strength in solar wind streams with different  $\sigma_c$  will be necessary to fully understand this phenomenon.

#### 4. DISCUSSION: IS RESIDUAL ENERGY RELATED WITH INTERMITTENCY?

Observing the Kurtosis in different runs, one immediately notices that Kurt( $\omega$ ) is smaller than Kurt( $J$ ) in all runs, implying magnetic structures are stronger than velocity structures. Consequently, one may conjecture that the negative residual energy is a result of intermittency. Bowen et al. (2018), using the WIND dataset, find that the negative residual energy is possibly related with intermittent structures in the magnetic field fluctuations. In top panels of Figure 5, we show time evolution of  $\sigma_r$  (black square) on top of the Kurtosis. One can see that as the simulation goes,  $\sigma_r$  decreases while the Kurtosis of both  $J$  and  $\omega$  increase. We note that in Bowen et al. (2018)'s observations, only Kurtosis( $J$ ) is negatively correlated with  $\sigma_r$  while there is very weak dependence of Kurtosis( $\omega$ ) on  $\sigma_r$ .

The top panels of Figure 5 suggest that intermittent structures and negative residual energy are simultaneously generated as the turbulence evolves. However, whether the negative residual energy is produced due to these intermittent structures is still unclear. To verify this point, we divide the simulation domain at the last frame ( $t = 200$ ) of each run evenly into  $16 \times 16 \times 16$  cubes, i.e. each cube contains  $32 \times 32 \times 32$  grid points. For each cube, we calculate Kurtosis( $J$ ), Kurtosis( $\omega$ ), and  $\sigma_r$ . Bottom left and bottom right panels of Figure 5 show the probability distribution of the data points for Run 2E and Run 2NE respectively. Black curves are the median values of the Kurtosis against the binned  $\sigma_r$ . In contrast with the top panels, in both the two runs (and the other runs whose results are similar and not shown here), Kurtosis( $J$ ) and Kurtosis( $\omega$ ) do not show significant correlation with  $\sigma_r$ . Although the data points spread widely in  $\sigma_r$ , the median values of the Kurtosis are quite constant. That is to say, at intermediate scales ( $L/16$ ), regions with negative residual energy do not necessarily correspond to intermittent structures.

Thus, we conclude that, in our simulations, negative residual energy and intermittency are simultaneously generated as a result of turbulence evolution, but the causal relation between them is weak. The reason is that the residual energy is concentrated at large scales (Figure 2) while the intermittent structures are generated at smaller scales. Our result indicates that the negative residual energy is more likely produced by the wave-wave interaction (Boldyrev et al. 2012b; Howes & Nielson 2013) combined with the expansion effect. Intermittent structures may slightly contribute to the negative residual energy, considering Kurt( $\omega$ ) < Kurt( $J$ ) in all the runs, but they are not very important. One explanation of the paradox between our simulations and satellite observations by (Bowen et al. 2018) is that Bowen et al. (2018) adopted large time windows (one hour) to



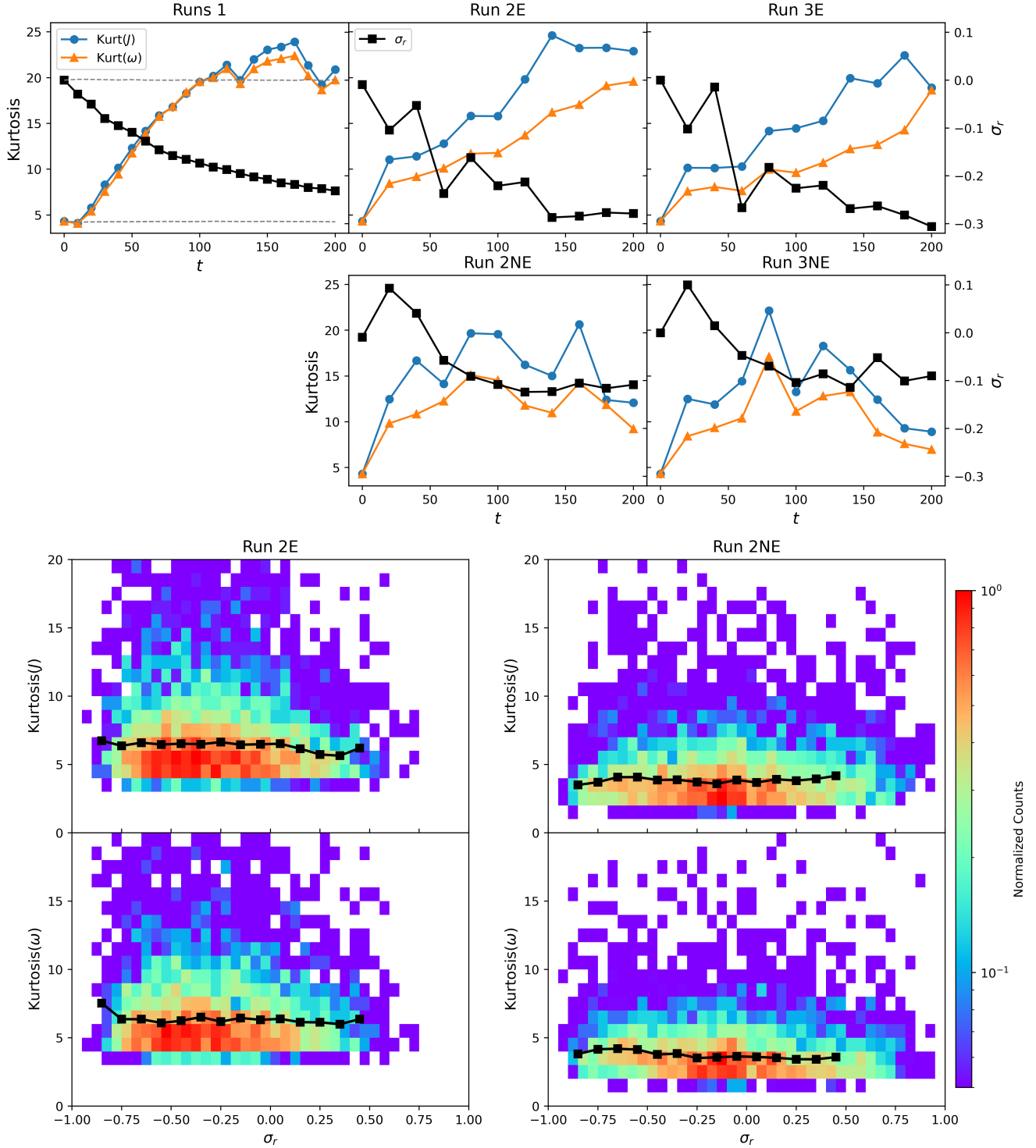


**Figure 5.** Top: Time evolution of Kurtosis( $J$ ) (blue circle), Kurtosis( $\omega$ ) (orange triangle), and  $\sigma_r$  (black square) in all the runs. Results from Run 1NE are shown as grey lines in the top left panel. Bottom: Probability distribution of Kurtosis( $J$ )- $\sigma_r$  (upper) and Kurtosis( $\omega$ )- $\sigma_r$  (lower) based on the last snapshot ( $t = 200$ ) of Run 2E. The simulation domain is divided into  $16^3$  equal-size cubes and these quantities are calculated for each individual cube. Black line is the median values of the Kurtosis against the binned  $\sigma_r$ . Right: Same as middle but for Run 2NE.

calculate these parameters and thus mixed large and small scales. However, we note that due to artificial

effects such as limited spatial resolution and lack of ki-

netic physics, the MHD simulations cannot capture all processes happening in the real solar wind.

## 5. SUMMARY

We conducted a set of 3D MHD simulations of solar wind turbulence with intermediate strength ( $|\delta\mathbf{b}|/B \sim 0.14$ ). The initial turbulence is Alfvénic, i.e. consists of counter-propagating Alfvén waves, and has zero residual energy and varying normalized cross helicity. The key results are summarized below:

1. Negative residual energy is always produced when nonlinear interaction takes effect, regardless of normalized cross helicity. The spherical expansion effect facilitates the generation of negative residual energy.
2. The magnetic field and velocity spectra are anisotropic and evolve differently. The magnetic field spectrum has a quite universal perpendicular slope of  $-3/2$  while the velocity spectrum is shallower. The negative residual energy has a spectrum  $-E_r \propto k_{\perp}^{-2}$  in most runs.
3. Spectral slope (perpendicular) of  $z^+$  (outward) is quite universal and slightly shallower than  $-3/2$ , while the spectral slope of  $z^-$  (inward) highly depends on  $\sigma_c$  when expansion effect is turned on such that the imbalanced turbulence has a steeper  $z^-$  spectrum. Without expansion,  $z^-$  spectrum

has a slope of  $-3/2$  for both the balanced run (Run 3NE) and imbalanced run (Run 2NE), .

4. Runs with expansion effect generate stronger intermittent structures in both magnetic field and velocity than the runs without expansion. The strength of intermittency does not show clear dependence on normalized cross helicity.
5. Growth of negative residual energy is accompanied by the generation of intermittent structures. However, the causal relation between the negative residual energy and intermittency is weak.

We emphasize that the strength of turbulence in our simulations is smaller than what is observed in the young solar wind, where  $|\delta\mathbf{b}|/B$  often reaches unity and thus magnetic “switchbacks” may form (Kasper et al. 2019; Bale et al. 2019; Tenerani et al. 2020, 2021). In addition, in the solar wind, the fluctuations are typically spherically polarized with  $|B| = \text{Const}$  (Matteini et al. 2018) while in the simulation it is hard to impose a spherically polarized fluctuation with a specified power spectrum. Nonetheless, it would be interesting and important to carry out simulations of random, spherically polarized fluctuations in the context of expanding solar wind, which will be a future study.

This study is supported by NSF SHINE #2229566 and NASA HTMS 80NSSC20K1275.

*Software:* Matplotlib (Hunter 2007)

## REFERENCES

- Artemyev, A., Shi, C., Lin, Y., et al. 2022, The Astrophysical Journal, 939, 85
- Bale, S., Badman, S., Bonnell, J., et al. 2019, Nature, 576, 237
- Belcher, J. 1971, Astrophysical Journal, vol. 168, p. 509, 168, 509
- Belcher, J., & Davis Jr, L. 1971, Journal of Geophysical Research, 76, 3534
- Beresnyak, A., & Lazarian, A. 2009, The Astrophysical Journal, 702, 460
- . 2010, The Astrophysical Journal Letters, 722, L110
- Boldyrev, S. 2005, The Astrophysical Journal, 626, L37
- Boldyrev, S., Perez, J. C., & Wang, Y. 2012a, arXiv preprint arXiv:1202.3453
- Boldyrev, S., Perez, J. C., & Zhdankin, V. 2012b, in AIP Conference Proceedings, Vol. 1436, American Institute of Physics, 18–23
- Bowen, T. A., Mallet, A., Bonnell, J. W., & Bale, S. D. 2018, The Astrophysical Journal, 865, 45
- Bruno, R., & Carbone, V. 2013, Living Reviews in Solar Physics, 10, 1
- Chandran, B. D., Schekochihin, A. A., & Mallet, A. 2015, The Astrophysical Journal, 807, 39
- Chen, C., Bale, S., Salem, C., & Maruca, B. 2013, The Astrophysical Journal, 770, 125
- Chen, C., Bale, S., Bonnell, J., et al. 2020, The Astrophysical Journal Supplement Series, 246, 53
- Cranmer, S. R., Asgari-Targhi, M., Miralles, M. P., et al. 2015, Philosophical Transactions of the Royal Society A: Mathematical, Physical and Engineering Sciences, 373, 20140148
- Cranmer, S. R., Van Ballegooijen, A. A., & Edgar, R. J. 2007, The Astrophysical Journal Supplement Series, 171, 520

- Dobrowolny, M., Mangeney, A., & Veltri, P. 1980a, *Solar and Interplanetary Dynamics*, 143
- . 1980b, *Physical Review Letters*, 45, 144
- Dong, Y., Verdini, A., & Grappin, R. 2014, *The Astrophysical Journal*, 793, 118
- D' Amicis, R., & Bruno, R. 2015, *The Astrophysical Journal*, 805, 84
- D' amicis, R., Matteini, L., & Bruno, R. 2019, *Monthly Notices of the Royal Astronomical Society*, 483, 4665
- Gogoberidze, G., Chapman, S. C., & Hnat, B. 2012, *Physics of Plasmas*, 19
- Goldreich, P., & Sridhar, S. 1995, *The Astrophysical Journal*, 438, 763
- . 1997, *The Astrophysical Journal*, 485, 680
- Grappin, R., Leorat, J., & Pouquet, A. 1983, *Astronomy and Astrophysics*, 126, 51
- Grappin, R., & Velli, M. 1996, *Journal of Geophysical Research: Space Physics*, 101, 425
- Grappin, R., Verdini, A., & Müller, W.-C. 2022, *The Astrophysical Journal*, 933, 246
- Heinemann, M., & Olbert, S. 1980, *Journal of Geophysical Research: Space Physics*, 85, 1311
- Howes, G. G., & Nielson, K. D. 2013, *Physics of Plasmas*, 20
- Hunter, J. D. 2007, *Computing in Science & Engineering*, 9, 90, doi: [10.1109/MCSE.2007.55](https://doi.org/10.1109/MCSE.2007.55)
- Iroshnikov, P. 1964, *Soviet Astronomy*, 7, 566
- Kasper, J. C., Bale, S. D., Belcher, J. W., et al. 2019, *Nature*, 576, 228
- Kraichnan, R. H. 1965, *The Physics of Fluids*, 8, 1385
- Lionello, R., Velli, M., Downs, C., et al. 2014, *The Astrophysical Journal*, 784, 120
- Lithwick, Y., & Goldreich, P. 2003, *The Astrophysical Journal*, 582, 1220
- Lithwick, Y., Goldreich, P., & Sridhar, S. 2007, *The Astrophysical Journal*, 655, 269
- Magyar, N., & Nakariakov, V. 2021, *The Astrophysical Journal*, 907, 55
- Mallet, A., & Schekochihin, A. A. 2017, *Monthly Notices of the Royal Astronomical Society*, 466, 3918
- Matteini, L., Stansby, D., Horbury, T., & Chen, C. H. 2018, *The Astrophysical Journal Letters*, 869, L32
- Montroll, E. W., & Shlesinger, M. F. 1982, *proceedings of the National Academy of Sciences*, 79, 3380
- Müller, W.-C., & Grappin, R. 2005, *Physical Review Letters*, 95, 114502
- Panasenco, O., Velli, M., D' amicis, R., et al. 2020, *The Astrophysical Journal Supplement Series*, 246, 54
- Parashar, T., Goldstein, M., Maruca, B., et al. 2020, *The Astrophysical Journal Supplement Series*, 246, 58
- Perez, J. C., & Boldyrev, S. 2007, *The Astrophysical Journal*, 672, L61
- . 2009, *Physical review letters*, 102, 025003
- Perez, J. C., Mason, J., Boldyrev, S., & Cattaneo, F. 2012, *Physical Review X*, 2, 041005
- Phillips, C., Bandyopadhyay, R., McComas, D. J., & Bale, S. D. 2023, *Monthly Notices of the Royal Astronomical Society: Letters*, 519, L1
- Réville, V., Velli, M., Panasenco, O., et al. 2020, *The Astrophysical Journal Supplement Series*, 246, 24
- Shi, C., Velli, M., Tenerani, A., Rappazzo, F., & Réville, V. 2020, *The Astrophysical Journal*, 888, 68
- Shi, C., Velli, M., Tenerani, A., Réville, V., & Rappazzo, F. 2022, *The Astrophysical Journal*, 928, 93
- Shi, C., Velli, M., Panasenco, O., et al. 2021, *Astronomy & Astrophysics*, 650, A21
- Shoda, M., Suzuki, T. K., Asgari-Targhi, M., & Yokoyama, T. 2019, *The Astrophysical Journal Letters*, 880, L2
- Sioulas, N., Shi, C., Huang, Z., & Velli, M. 2022a, *The Astrophysical Journal Letters*, 935, L29
- Sioulas, N., Velli, M., Chhiber, R., et al. 2022b, *The Astrophysical Journal*, 927, 140
- Sioulas, N., Huang, Z., Velli, M., et al. 2022c, *The Astrophysical Journal*, 934, 143
- Sioulas, N., Huang, Z., Shi, C., et al. 2023, *The Astrophysical journal letters*, 943, L8
- Tenerani, A., Sioulas, N., Matteini, L., et al. 2021, *The Astrophysical Journal Letters*, 919, L31
- Tenerani, A., & Velli, M. 2017, *The Astrophysical Journal*, 843, 26
- Tenerani, A., Velli, M., Matteini, L., et al. 2020, *The Astrophysical Journal Supplement Series*, 246, 32
- Van Ballegooijen, A., & Asgari-Targhi, M. 2016, *The Astrophysical Journal*, 821, 106
- Velli, M., Grappin, R., & Mangeney, A. 1991, *Geophysical & Astrophysical Fluid Dynamics*, 62, 101
- Verdini, A., Velli, M., Matthaeus, W. H., Oughton, S., & Dmitruk, P. 2009, *The Astrophysical Journal Letters*, 708, L116
- Wang, Y., Boldyrev, S., & Perez, J. C. 2011, *The Astrophysical Journal Letters*, 740, L36
- Wu, H., Huang, S., Wang, X., et al. 2023, *The Astrophysical Journal Letters*, 947, L22
- Yokoi, N., & Hamba, F. 2007, *Physics of Plasmas*, 14